Investigating the Role of Plasmonics in Electrospun Fibers by Combined Photothermal Heterodyne Imaging and Raman Measurements

Yechan Moon, Susan V. Olesik*, Zachary D. Schultz*

Department of Chemistry and Biochemistry, The Ohio State University, Columbus, Ohio 43210, United States

*Corresponding author emails: olesik@chemistry.ohio-state.edu, schultz.133@osu.edu

Abstract

The addition of plasmonic nanoparticles into electrospun polymer fibers can have significant impact on their properties relevant to applications in sensing, catalyst, and energy conversion. A Raman spectrometer incorporated into a photothermal heterodyne imaging system was used to study the hot electron transfer mechanism generated through excitation of a localized surface plasmon resonance (LSPR) of gold and silver nanoparticles in polyacrylonitrile films and nanofibers. The ratio of anion nitrile radicals to neutral nitriles of polyacrylonitrile, provides a measure of the ionization capabilities of the nanoparticles, was found to follow a Boltzmann distribution, indicating that the LSPR mediated hot electron transfer mechanism is dependent on temperature. Silicon nanoparticles were used as a control for temperature and showed that heating itself, using 405 nm and 532 nm pump lasers, was not sufficient to ionize polyacrylonitriles, even at relatively high temperatures. The results provide insight into the roles of heating and electron transfer arising from nanoparticles additives in electrospun polymer fibers and other materials.

Introduction

The uses for nanofibers have steadily increased over the years due to their unique properties like flexibility, mechanical strength, high surface area to volume/weight ratio, porosity, sample loading capacity, reproducibility, and ability to incorporate nanomaterials to change the electrical and heat conductivity without fiber degradation. Because of this, nanofibers have been utilized in applications like: flexible electronics,[1–3] lithium ion battery cathodes and anodes,[4–7] surface assisted laser desorption/ionization (SALDI) substrates,[8–12] catalysts,[13–16] and solar cells.[17–19] The most common method to produce these nanofibers is through electrospinning.

Plasmonic nanomaterials, which can be incorporated into nanofibers, are known to exhibit a localized surface plasmon resonance (LSPR).[20] The LSPR occurs when an incident beam of light interacts with the electrons in the conduction band of the plasmonic nanomaterials. This interaction produces a plasmonic oscillation with a resonant frequency specific to the size, geometry, dielectric environment, and the composition of the material. The resulting effect is an enhancement of the local electric field which is credited for the underlying mechanism in surface enhanced Raman spectroscopy (SERS). SERS is a powerful technique reported in literature to enhance Raman signals up to $10^8 \sim 10^{10}$ times.[21–23] While the enhancement of the electric field arises from the radiative decay of the plasmonic oscillation, hot electrons are produced through a non-radiative process. Hot electrons and carriers are generated in a nonthermal distribution and are damped in 1-100 femtoseconds. Hot carrier relaxation, where the population of hot electrons and hot holes redistributes its energy through electron-electron interactions last up to 1 picosecond, is followed by thermal dissipation to the surrounding from the particle within 10 nanoseconds.[24–27] Since the electron-electron interactions occur extremely fast, only high potential energy hot electrons are expected to undergo electron transfer.[28]

Nitriles, exhibiting a unique vibrational peak in the silent region (1750 cm^{-1} to 2750 cm^{-1}), have been used as a probe for experimentally measuring the vibrational Stark effect and electronic charging observed in SERS experiments.[29–34] The vibrational Stark effect arises from charge differences associated with exciting the LSPR.[35] Optical rectification results in a local DC field, affecting the electric fields experienced by the chemical bonds and evident as a shift in the vibrational frequency observed in SERS. Previously, Wang et el. reported a shift of approximately 100 cm^{-1} wavenumbers on 4-mercaptobenzonitrile, a shift too large to be accounted for a vibrational Stark effect.[34] Using alkane thiols to form a controlled spacing between gold nanoparticles and gold film, it was shown that larger distances decreased the magnitude of the vibrational shift, but not the direction of the shift. This phenomenon was attributed to an electron transfer induced peak shift and was backed through computational calculations. With this knowledge, electron transfer phenomena associated with the LSPR can be measured through changes in the vibrational spectrum of nitrile probe molecules.

The relaxation of the plasmon resonance also results in local heating from the nanoparticle to the surrounding medium. Photothermal heterodyne imaging (PHI) can be used to study this local heating from plasmonic nanomaterials.[36–40] PHI measures the change in refractive index of the sample arising from the change in temperature caused by absorption of a pump beam. The absorption of the modulated pump beam induces a temporal thermal response, giving rise to a modulated change in the refractive index of the sample. The modulated intensity of the probe beam, co-aligned with the pump beam, is recorded and demodulated with a lock-in amplifier.

In this report, the relationship between heating and hot electron generation of plasmonic nanoparticles in polyacrylonitrile film and fibers is studied through simultaneous Raman spectroscopy and PHI measurements. Gold and silver nanoparticles were investigated due to their excellent plasmonic properties and compared to non-plasmonic silicon nanoparticles in polyacrylonitrile films and fibers. Formation of the nitrile anion was only observed when plasmonic nanoparticles were included, and a higher degree of ionization correlated with increased PHI intensities. The result indicates that although LSPR is the responsible for ionization, it is facilitated through heating. We also report the ionization efficiency differences of the plasmonic nanoparticles in film compared to their fiber counterparts, suggesting that the chemical environment and potential nanoparticle aggregation affects the ionization capabilities of plasmonic nanoparticles.

Materials and Methods

Materials

Polyacrylonitrile (PAN, M_w 150,000) was purchased from Sigma-Aldrich (St Louis, MO) and dimethylformamide (DMF) was purchased from Fisher Scientific (Fairlawn, NJ). Dried gold and silver nanoparticles (50nm, 40 kDa PVP as capping agent) were purchased from NanoComposix (San Diego, CA), and silicon nanoparticles (50nm, dried) were purchased from Sky Springs Nanomaterials, Inc. (Houston, Tx).

Instruments

An Agilent Cary 4000 UV-Vis spectrometer was used to measure the extinction spectrum of gold, silver, and silicon nanoparticles in ethanol. FEI Tecnai G2 Spirit transmission electron microscope (TEM) was used to image the nanoparticles imbedded inside the electrospun PAN nanofibers.

Electrospinning Nanofibers

PAN powder was dissolved in DMF and stirred over night to make a 10% (w/w) polymer solution. To incorporate nanoparticles, 2%, 1% and 0.1% (w/w to PAN) of gold, silver, or silicon was sonicated in DMF before the addition of PAN. The polymer solution was then transferred to a plastic syringe, capped with a stainless-steel needle. Harvard Apparatus Pump II Elite (Holliston, MA) syringe pump was used to deliver the solution for electrospinning. Spellman CZE 1000R (Hauppauge, NY) power supply was used to deliver the positive voltage to the needle tip and to ground an indium-tin-oxide (ITO) coated glass (Sigma-Aldrich, MO). Electrospun polymer nanofibers were collected for 5 minutes at a collection distance of 15 cm with a flow rate of 1 ml/hour. Voltage was set to 15 kV and provided an average fiber diameter of 398 ± 74 nm for bare PAN nanofibers, and 205 ± 45 nm, 364 ± 52 nm, and 251 ± 52 nm for gold, silver, and silicon incorporated PAN fibers, respectively. (See **Figure S1** and **S2** in the SI for images of nanofibers) Nitrogen gas was used reduce the relative humidity to less than 20%. A diagram of the electrospinning setup is included in **Figure S3**. PAN films were made by air drying a drop of the electrospinning solution on a glass slide.

Photothermal Heterodyne Imaging (PHI) Setup

A previous reported photothermal heterodyne imaging setup[39,41] was modified for this experiment. The current PHI setup is adapted onto a dual microscope designed by Nanonics Imaging, LTD and operated in transmission mode with a 50x air objective (NA = 0.5 Olympus, LMPLFLN50xBD) focusing lens and a 50x air objective (Nikon NA = 0.45, WD = 17 mm) collection lens. Setup of the modified instrument is shown below in **Figure 1**.

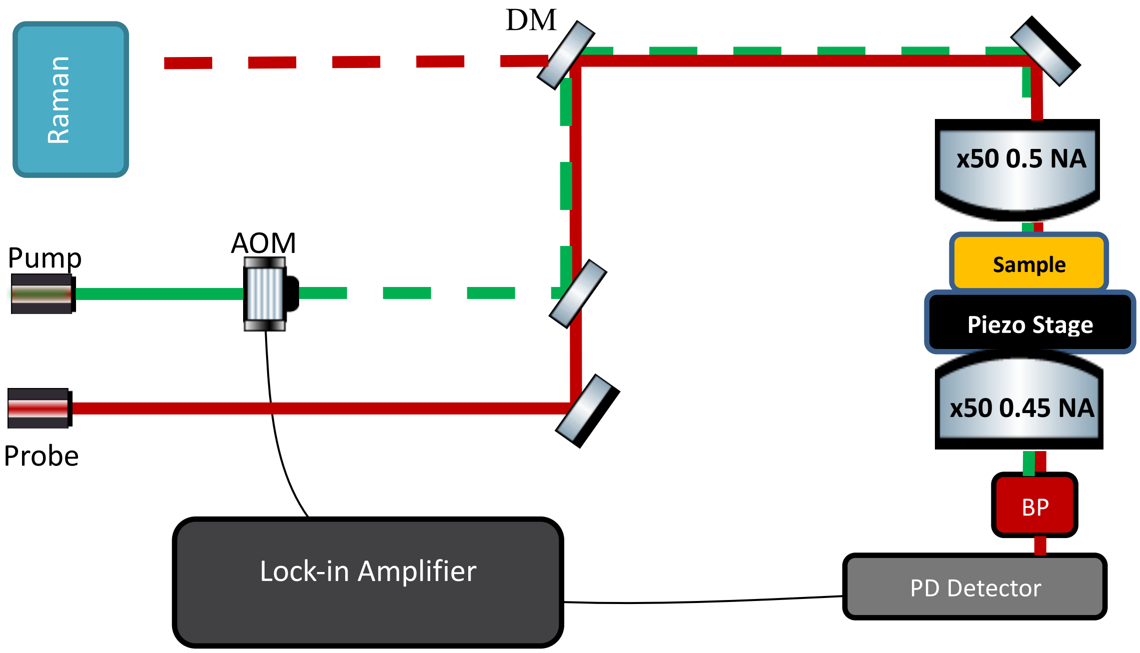

Figure 1. PHI with SERS microscopy instrument setup. The following abbreviations are as follows: AOM = Acousto-optic-modulator, DM = Dichroic mirror, BP = Band pass filter.

The pump beam, either as 405 nm (RPMC, LBX-405) or a 532 nm (Innovation Photonic Solution, I0532sl0100MF) cw-laser is modulated by an acousto-optic-modulator (Gooch and

Housego, AOMO 3200-124) at a rate of 400 kHz. The He-Ne 633nm probe beam (Melles Griot, 25-LHP-925) was aligned and focused and overlapped with the pump beam through a long-pass dichroic mirror (4, Thorlabs, DMLP567). Since the probe beam is used for detection, the setup is diffraction limited by the probe beam. A Nanonics-MV4000 piezo stage scanner was used to move the sample in the xyz directions for imaging. Ideally, the modulated pump beam is absorbed by the sample, which causes heating, resulting in a modulated refractive index change $\left(\frac{dn}{dT}\right)$ of the sample. Due to the alignment of the two beams, the modulated refractive index change of the sample also modulates the intensity of the probe beam detected by the photodiode at the same frequency as the pump beam. A band pass filter (Thorslab, FB650-40) was used to selectively filter out the pump beams to only allow the probe beam to reach a custom photodiode detector.[41] The lock-in amplifier (Stanford Research Systems, SR844) then demodulates the photothermal signal of the probe beam. All PHI images were collected at 0.3 mW pump beam and 0.5 mW pump beam unless indicated otherwise.

The Raman spectrum was recorded by measuring the scatter from the 633 nm probe beam using a spectrometer (Andor SOLIS, SR328i) and CCD (Andor iDus DU416A-LDC-DD) incorporated into the PHI setup. The Raman mapping was sampled at 17 x 17 pixels with 5 second acquisitions. The PHI image was collected over a 10 x 10 μm^2 area containing 100 x 100 pixels with 50 millisecond acquisitions per pixel. Both images were collected at the same time using Combridge component in NWS11 v1.0_06_08_17 (Nanonics Imaging, LTD), collecting PHI signals line by line while collecting the Raman spectrum at defined points in the scan.

Results and Discussion

The photothermal response of the sample has a wavelength dependence that requires selecting the appropriate pump and probe beam wavelengths. **Figure 2** shows the extinction spectra of nanoparticles and polyacrylonitrile fibers studied here. The absorption maxima were observed at 533 nm, 435 nm, and 405 nm for 50 nm gold, silver, and silicon nanoparticles, respectively. To maximize absorption, a 532 nm or 405 nm laser was used as the pump beam. The probe beam at 633 nm shows minimal absorption to correlate heating of the sample to the pump beam and serving as the Raman excitation source. While aggregation can induce a red-shifted coupled plasmon resonance, it has been shown that this band diminishes in larger aggregates (more than 2 nanoparticles), which will diminish resulting heating.[42] Silicon nanoparticles are included, as they show an absorption at comparable wavelengths but do not form a plasmon resonance like Ag and Au nanoparticles. PAN has its peak absorption at 316 nm and has minimal response to the 405 nm and 532 nm pump beams of the PHI system (**Figure S4, S5, S6, and S7**).

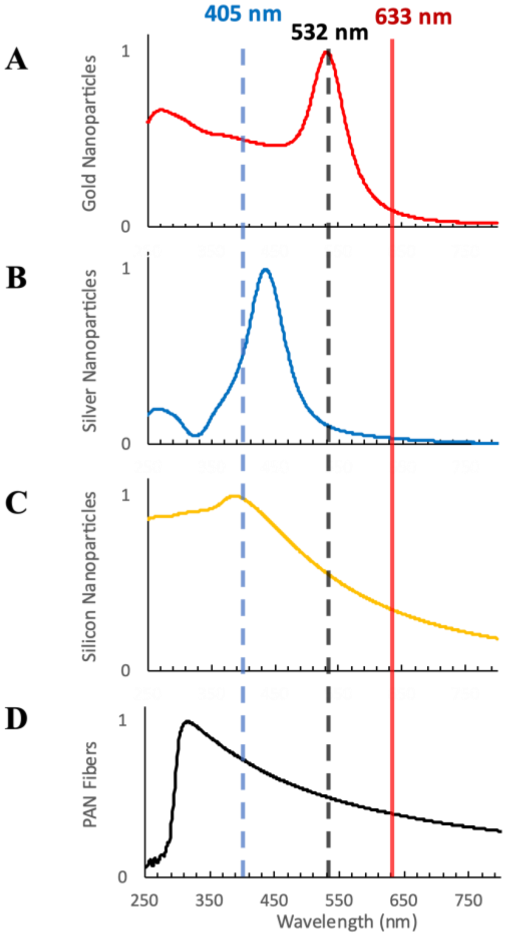

Figure 2. Extinction Spectra of gold (A), silver (B), and silicon (C) nanoparticles and polyacrylonitrile fibers (D). The vertical dashed lines indicate the wavelength of the pump beams (405 nm and 532 nm) used in the photothermal heterodyne system. The solid line (633 nm) indicates the wavelength of the probe beam and Raman, which has relatively minimal absorption from the nanoparticles and fibers.

To monitor potential electron transfer events, the nitrile moiety on the polyacrylonitrile fibers and film was studied. While polyacrylonitrile has many distinct Raman peaks, the nitrile stretch at 2245 cm^{-1} is readily distinguishable within the vibrationally silent region (1750 cm^{-1} to 2750 cm^{-1}). As noted in the introduction, nitrile peaks are experimentally observed red-shifted by around 100 cm^{-1} with an addition of an electron, [43] which was confirmed by constrained density functional theory (CDFT) calculations.[34]

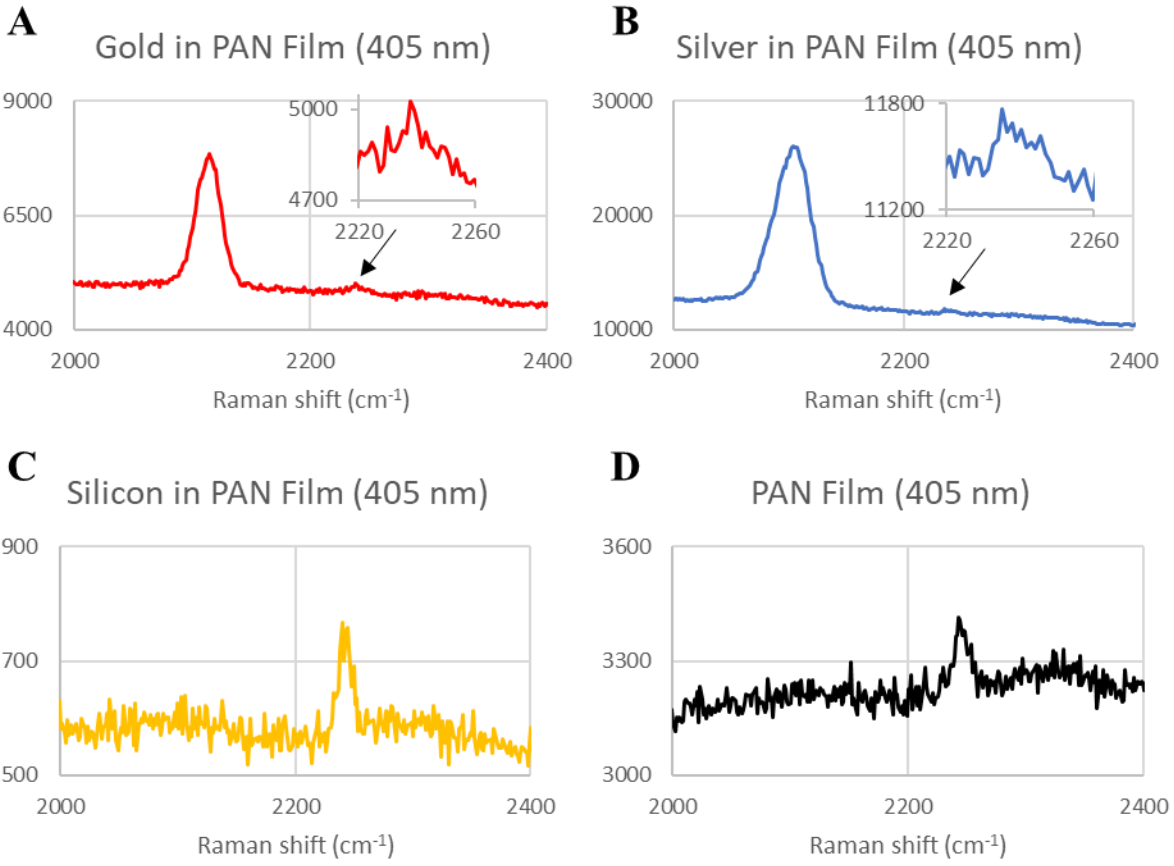

Figure 3. Raman spectra a PAN film containing of gold **(A)**, silver **(B)**, silicon **(C),** and no **(D)** nanoparticles while illuminated by the 405 nm modulated pump beam in the photothermal heterodyne imaging setup. The spectra were collected using the 633nm probe beam with a 5 s acquisition and 0.5 mW power.

Figure 3 shows the Raman spectrum of PAN with the addition of gold, silver, and silicon nanoparticles obtained simultaneously during at PHI experiments with the 405 nm pump beam. A low intensity nitrile stretch is observed in all samples. The anion nitrile radical band is only observed in PAN fibers and films incorporating plasmonic nanoparticles (2120 cm^{-1} and 2016 cm^{-1} for gold and silver, respectively). Enhancement of Raman signals of nitriles with gold and silver nanoparticles is due to SERS, which arises from the excitation of the nanoparticles' LSPR.

In all cases, the SERS is measured from the 633 nm probe beam. The Raman signal observed from both Ag and Au nanoparticles is significantly enhanced (>100x) relative to the nitrile signal from the silicon or bare PAN films which shows more modest Raman signals. The spectra shown were collected with the same incident powers, enabling this direct comparison. A remnant of the original nitrile peak, comparable in intensity to that observed in PAN and with Si nanoparticles, is still evident in the Raman spectrum of PAN with silver and gold nanoparticles as indicated with the arrows in **Figure 3**. While quantifying the SERS signal between samples is challenging due to known heterogeneity in the plasmonic enhancement, having information of both the uninterrupted nitrile and nitrile anion radical peaks allow for an internally standardized ratio of the two peaks. The ratio can be used to quantitatively assess the electron transfer events observed near the nanoparticles.

The photothermal heterodyne imaging signal was recorded by detecting the modulated change in the intensity of the probe beam at the detector. The modulation occurs due to the refractive index change caused by the temperature change of the sample through the absorbance of the modulated pump beam. **Figure 4.A** shows the PHI of PAN film with silver nanoparticles under a 405 nm pump beam. An enlarged image can be found in **Figure S6**.

The bright spots in **Figure 4A** correspond to the absorbance of the pump beam which leads to local heating and the refractive index change. The increased absorption cross section of the nanoparticles generates more heat and a larger change in the refractive index of the sample that readily indicates the presence of nanoparticles. Previous results have shown that the PHI intensity is linear to the volume of the nanoclusters,[39] meaning that larger nanoparticle clusters will dissipate more heat in the diffraction limited area. The intensity scale of the PHI is proportional to the lock-in amplifier gain, the absorption cross sections of the sample, and optical collection efficiency. Using consistent collection conditions, the signal can compare the relative amount of heating between samples induced by the pump beam. PHI images of other substrates can be found in the **Figures S4-S7**.

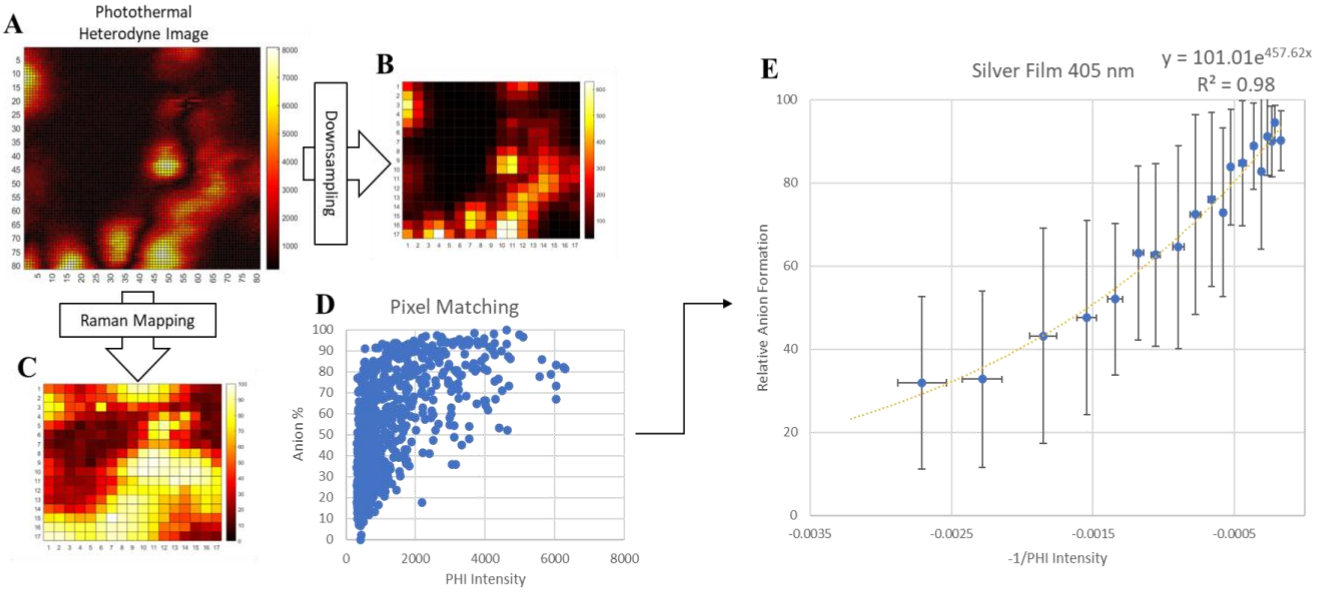

Figure 4. The flow chart shows the data processing to correlate the heating measured by PHI to the anion nitrile radical formation observed by Raman. **(A) The** PHI of silver nanoparticles in polyacrylonitrile film is shown. The color bar correlates to the observed PHI signal. **(B)** The downsampled map of PHI from (A) is correlated with the anion ratio in **(C)** the Raman map. The anion ratio was determined by **Eq.1** at each Raman point. **(D)** A scatter plot shows the pixel matching correlating the PHI intensity and anion nitrile radical population from maps (B) and (C)**. (E)** The average anion% from (D) at each PHI value is plotted and fit to a Boltzmann distribution.

To quantitatively compare the heating and anion formation (a proxy for electron transfer) induced by the pump beam with the different nanoparticles, the correlated PHI and Raman signal (**Figure 4E**) was modeled as a two state population (neutral nitrile and anion nitrile radical) and rearranged to calculate relative anion formation using the following **Equation 1**:

$$Relative\ Anion\ Formation = \frac{Ionized\ Nitrile}{Total\ Nitrile} \times 100\% \qquad (1)$$

The photothermal image was downsampled to match the pixel denisty of the Raman map (17 x 17, 8 x 8 μm) for a pixel by pixel analysis. The combined PHI-Raman analyses from four separate images per sample were combined and fit to a Boltzmann distribution. **Figure 4** illustrates the overall data processing applied across all the samples. The Boltzmann distribution equation (**Equation 2**) was modified to represent relative anion formation (**Equation 3**):

$$p_{Anion} = \frac{1}{Q}\exp\left(\frac{-\varepsilon_{Anion}}{kT}\right) = \frac{\exp\left(\frac{-\varepsilon_{Anion}}{kT}\right)}{\sum_{j=1}^{M}\exp\left(\frac{-\varepsilon_{Anion}}{kT}\right)} \tag{2}$$

$$Relative\ Anion\ Formation = \frac{100}{Q}\exp\left(\frac{-\varepsilon_{Anion}}{kT}\right) \tag{3}$$

Where ε_{Anion} is the energy associated with the formation of anion nitrile radical species, p_{Anion} is the probability of the anion nitrile radical state, k is the Boltzmann constant, T is the absolute temperature, M is the total number of states (2 in this case), and Q is a normalization factor. Photothermal signals have been shown to be linearly correlated with the change in the local temperature and can is described by the following equation[40,44]:

$$PHI = \frac{1}{\pi\omega_0} n \frac{\partial n}{\partial T}\frac{1}{C_p\lambda^2\Omega}\frac{\sigma_{abs}}{A}P_{pump}P_{probe}\Delta t \tag{4}$$

ω_0 is the probe beam focal radius (beam waist), n and $\frac{\partial n}{\partial T}$ is the refractive index and the temperature coefficient of refractive index of the medium, C_p is the heat capacity of the photothermal medium (PAN), Ω is the modulation frequency, A is the diffraction limited area ($\frac{\lambda}{2NA}$), λ is the wavlength of the probe beam, Δt is the integration time by the lock in amplifier. The P_{pump} and P_{probe} are the power of the modulated pump and probe beams respectively. Since the experimental conditions across samples are not changed, the only variable of interest is now σ_{abs}, which is essentially the absorption coefficient of the nanoparticles. At the wavelengths investigated, the absorption coefficient of the nanoparticles is significantly larger than the PAN, such that the PAN can be ignored. Since the PHI response is linear to the temperature change caused by absoprtion of the pump beam, the electron transfer response to PHI signal can now be represented when comparing across different samples as follows:

$$Relative\ Anion\ Formation = A \exp\left(B \frac{1}{-PHI}\right) \qquad (5)$$

where A is the saturation, which should theoretically be 100, and $B = \frac{\varepsilon_{Anion}}{k}$. Utilizing this new model, **Figure 5** shows the correlation between electron transfer and heating of nanoparticles in PAN films on glass slides.

As shown in **Figure 5D**, the PAN film does not show a dramatic increase in the PHI signal, indicating a lack of absorbance of the 405 nm pump beam. The silicon incorporated film shows high values of PHI signal intensities, but the lack of ionization indicates that pump induced heating itself is not enough to produce hot electrons to transfer to the nitriles in PAN. Gold and silver nanoparticles show a high degree of electron transfer to PAN and follow the two state Boltzmann distribution model with the increase in the intensity of the PHI signal. The exponent component of the fits is lower for gold than silver, suggesting the processes require less energy with the gold nanoparticles. The increased PHI signal indicates that heating facilitates the electron transfer with plasmonic nanoparticles. The same analysis was done with electrospun PAN nanofibers. Gold and silver nanoparticles in electrospun PAN fibers follow the same trend, as observed in PAN films. Interestingly, our data show that the fibers require lower energy (smaller exponents in the Boltzman fit) to form the anion nitrile radical state, suggesting that anion formation may be favored in the fibers compared to the films.

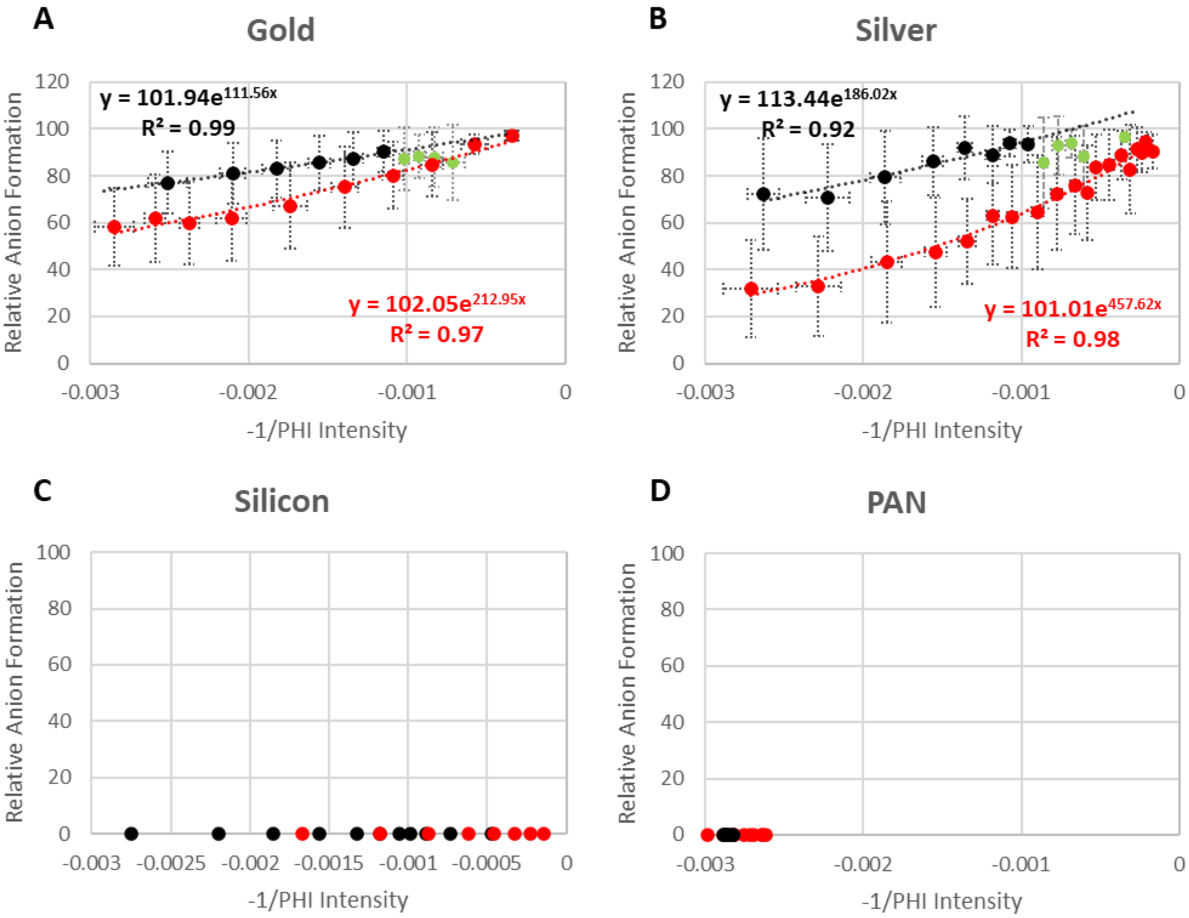

Figure 5. The plot of -1/PHI intensity vs Anion % for gold **(A)**, silver **(B)**, silicon **(C)**, and no **(D) nanoparticles** in PAN fibers **(black)** and films **(red)**, observed with a 405 nm pump beam in the PHI measurement. The green points indicate cyclization reaction of PAN, proposed in **Figure 8A**.

One explanation for the preferred anion formation in the fibers could be the difference in molecular orientation of the substrates. Orientation can effect the ionization capabilities of the nanoparticles and possibly the refractive index of PAN. The orientation of electrospun nanofibers have been shown to be more ordered on the outside of the fiber compared to the films,[45–48] but the nanoparticles are shown to be in the inside (**Figure 6**) so molecular orientation alone cannot explain the huge difference in the energy states. Another possible explanation is the different aggregation states of the nanoparticles. Aggregation of the nanoparticles occurs when the attractive forces between nanoparticles, mainly van der Waals, dominate over repulsive forces like electrostatic forces and steric interactions.[49] Since electrospinning requires high voltages, nanoparticles that are electrospun often aggregate differently than those in films. This difference arises from the applied voltage polarizing the polymer solution, causing nanoparticles to be positively charged on one side and negatively on the other, allowing for linear alignment and aggregation due to electrostatic attractions between nanoparticles.[50] Conversely, nanoparticles in drop-cast films show signs of random clustering. Liu, et al. showed that gold nanoparticles, less than 10 nm diameter, decreased in efficiency for hot carrier generation with size.[51,52] The change in carrier generation with size may support decreased efficiency in randomly clustered aggregated compared to the regular alignment in fibers. SERS experiments using nanoclusters have shown optical rectification to occur that is evident through a slight shift in the CN stretch arising from the Stark effect.[35,53] This Stark shift occurs due to the polarization of charges within nanojunctions, forming a quasi DC field. If this DC-field is the case, it could affect the electron transfer capabilities of aggregated nanoparticles.

Confinement within the nanofibers may also contribute to the difference between the film and the fibers. As shown in **Figure 6**, less PAN is locally availiable for heat dissipation and electron transfer of the aggregated nanoparticles in fibers. The lack of heat dissipation allows the PAN close to the nanoparticles and heat up faster, resulting in faster ionization.

Results in **Figure 5** indicate that gold nanoparticles are more efficient than silver nanoparticles as a hot carriers. This efficiency difference is the opposite of what one might expect, due to silver nanoparticles having stronger plasmon resonances[54] and higher frequency, which aligns more closely to the 405 nm pump beam than the plasmon frequency of gold (**Figure 2**). Besteiro et al. report that silver nanoparticles are four times more efficient at

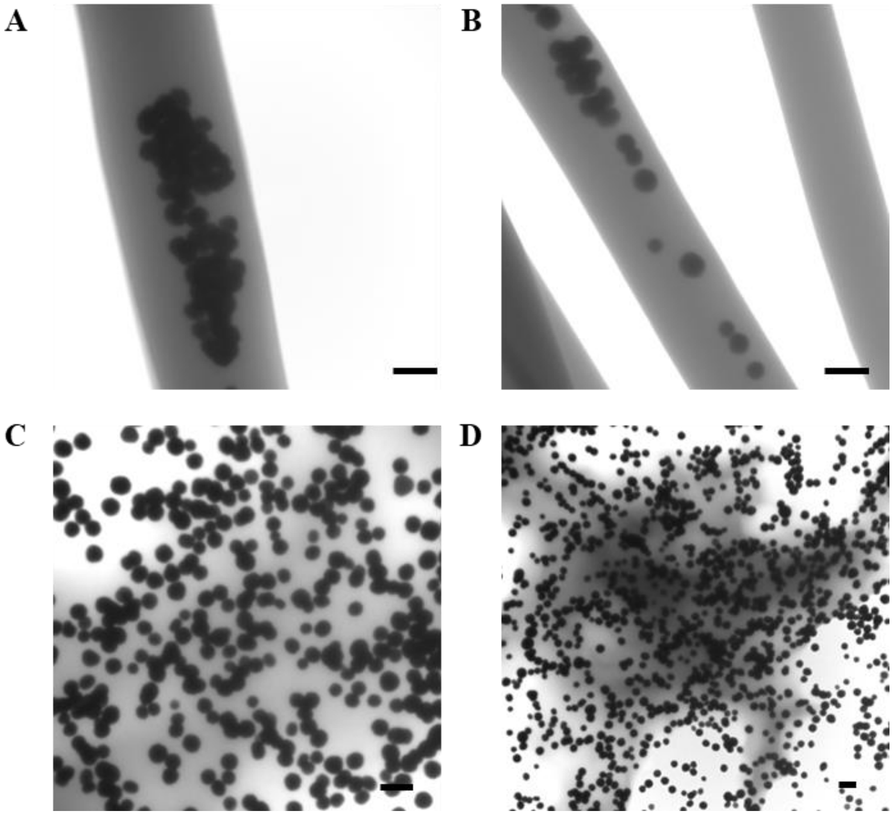

Figure 6. TEM images of silver **(A)** and gold **(B)** nanoparticles in electrospun PAN fibers. **(C)** and **(D)** show silver and gold nanoparticles drop cast on the TEM grid, respectively. Scale bars indicate 100 nm.

generating hot electrons than gold nanoparticles.[55] Note that the silver nanoparticles appear more prone to aggregation compared to gold nanoparticles in the electrospun fibers (**Figure 5A** and **5B,** respectively). The results indicate that aggregation of nanoparticles may matter more than the chemical differences between gold and silver nanoparticles.

Environmental factors, such as chemical interactions[56] between the nitriles and nanoparticles may also contribute to the less prevalent formation of anion nitriles on the silver nanoparticles. Another potential factor is the oxide formation on the surface of the silver nanoparticles, which can inhibit hot electron transfer between the metal and nitrile moieties of PAN. Oxygen reduction on the silver nanoparticles could compete for hot carriers and contribute to the oxide layer.[57,58]

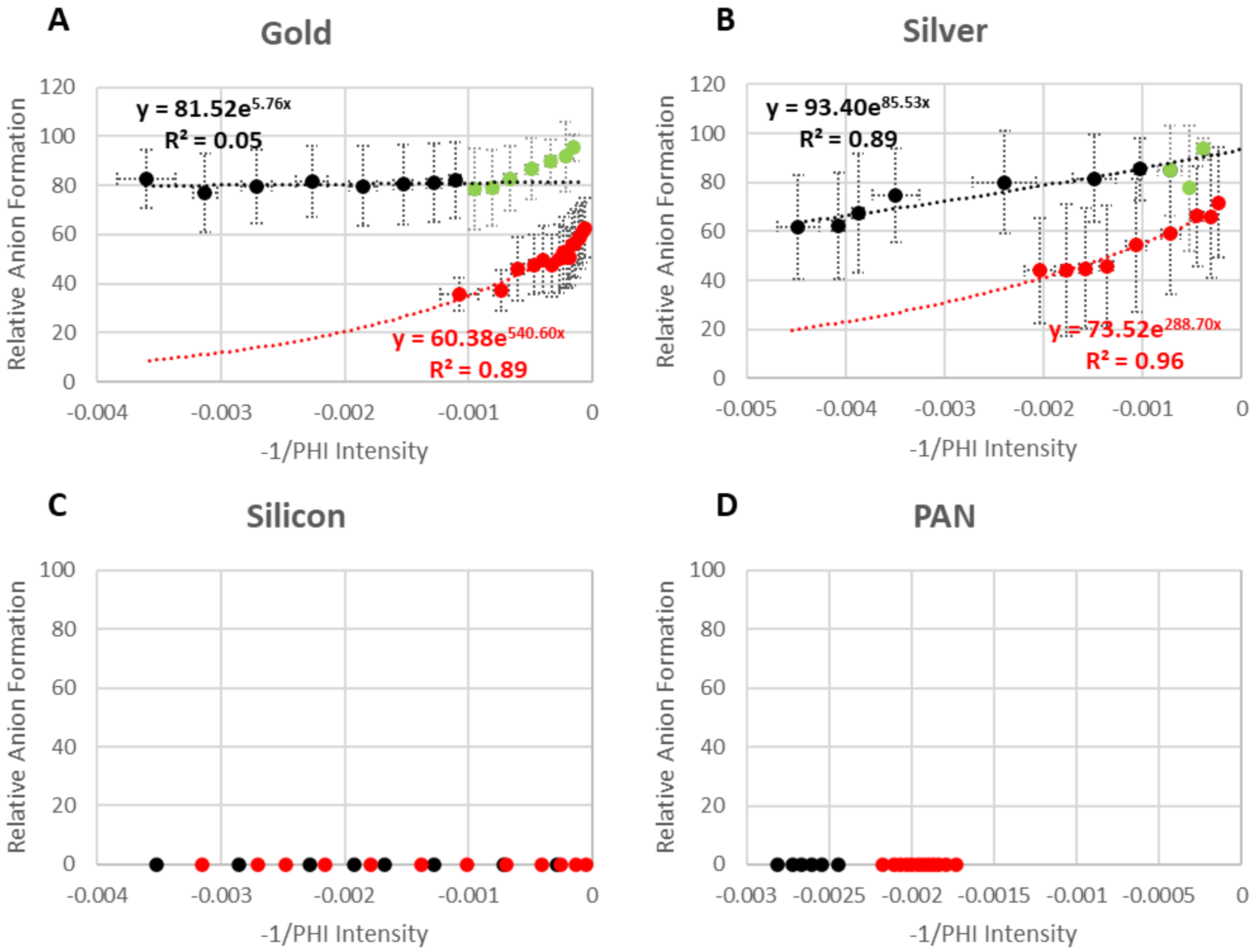

Figure 7. The plot of -1/PHI intensity vs Anion % for gold **(A)**, silver **(B)**, silicon **(C)**, and no **(D)** nanparticles in PAN fiber **(black)** and films **(red)**, observed with a 532 nm pump beam for the PHI measurement. The green points indicate cyclization reaction of PAN, proposed in **Figure 8A**.

To compare the ionization efficiency of plasmonic nanoparticles at a lower pump beam energy, a 532 nm pump beam was investigated. The lower energy laser is expected to decrease the ionization efficiency of the plasmonic nanoparticles, which agrees with **Figure 7** where the preexponential *A* value does not reach 100%. The 532 nm pump laser does not show evidence of ionization or heating in the PAN film without nanoparticles under the conditions used here. Silicon nanoparticles still result in heating, but no ionization is observed. Gold and silver nanoparticles show a degree of ionization, which increases as the relative temperature increases.

Gold nanoparticles in the nanofibers on the other hand, start at a higher anion percentage and the relative anion fraction does not seem to increase with temperature, indicating saturation of anion nitrile radical formation at a much lower temperature.

In **Figure 7**, the green portion of the data observed from the fibers does not fit with the two state Boltzmann distribution. The deviation from the Boltzmann model may be explained by the well-known cyclization of PAN, which is a structural change in PAN occurring at temperatures between $180°\mathrm{C}$ and $250°\mathrm{C}$.[59] This cyclization is a dehydrogenation reaction, transforming the $\mathrm{C} \equiv \mathrm{N}$ triple bond into a ring structured $\mathrm{C} = \mathrm{N}$ double bond, and will affect the nitrile population approximated in **Eq 1**. The reaction mechanism proceeds as shown in **Figure 8A**. Silver nanoparticles appear to catalyze this reaction, with the cyclization reaction occurring at a lower temperature than in the absence of the silver particles, and beginning graphitization at $200°\mathrm{C}$.[60]

Figure 8 shows the Raman spectra of PAN films incorporating either silver, gold, or silicon nanoparticles at a relatively high temperature. The spectra were selected from pixels showing high PHI intensity [PHI >5000, equivalent to (-1/PHI) > -0.0002]. Raman peaks at 1598 cm^{-1} and 1096 cm^{-1} are observed when silver nanoparticles are incorporated into PAN films. These peaks correspond to the formation of C=N and C=C ring structures, which are not evident in the other nanoparticle incorporated films. The 480 cm^{-1} band in the silicon incorporated PAN film corresponds to the silicon oxide band, found on the outer layers of the silicon nanoparticles. With the assumption that the same PHI intensities of different samples are equal in temperature, our data are consistent with silver catalyzing cyclization. While silicon nanoparticles heat more (show higher PHI intensity) than silver and gold nanoparticles, no cyclization was detected by Raman in the silicon nanoparticle samples.

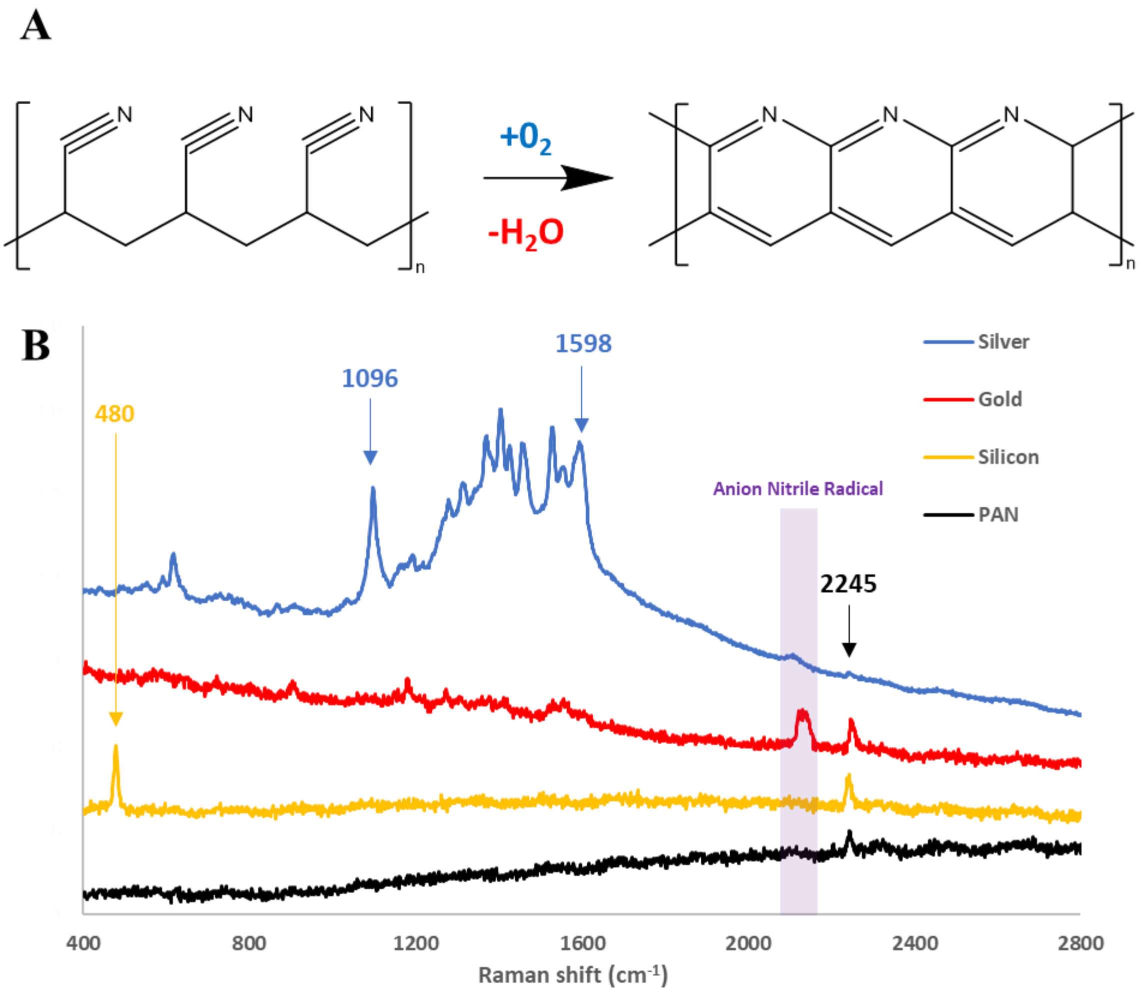

Figure 8. **(A)** The reaction mechanism for the dehydrogenation and cyclization of PAN to cyclized ring structure is shown. **(B)** Raman spectra are shown from PAN films incorporating silver **(blue)**, gold **(red)**, and silicon **(yellow)** nanoparticles and a PAN film **(black)**, collected during a PHI measurement with a 532 nm pump beam and 633 nm probe beam. The spectrum was collected from a bright region (PHI > 5000; -1/PHI > -0.0002) from the PHI map, indicating a relatively high temperature profile. The emergence of new peaks in silver supports a cyclization reaction.

Conclusion

A combined photothermal heterodyne imaging and Raman setup was utilized to study the relationship between the heating and hot electron transfer efficiency of plasmonic nanoparticles. Polyacrylonitrile (PAN) was used as a matrix due to nitriles acting as a good internal calibrant (ionized nitrile vs non-ionized nitrile) for SERS. Our data shows that heating of plasmonic nanoparticles (gold and silver) produces more radical anion nitriles, indicating that the rate of hot electron transfer is affected by the temperature of the nanoparticles. Silicon nanoparticles, which lack a LSPR and associated induced hot carriers, do not show signs of electron transfer, even at higher relative temperatures. PAN films and fibers were compared to assess the impact of structure on the heating and ionization from the plasmonic nanoparticles. The results show easier heating and ionization of the particles in fibers, but a rapid heating environment causes unwanted cyclization reaction of PAN which affects the model used to compare the ionization efficiency of the nanoparticles. The results suggest that differences in the chemical environment and possible aggregation of the nanoparticles could explain discrepancies with existing models. It is postulated that aggregation affects the nitrile anion formation efficiency with plasmonic nanoparticles, where more dispersed nanoparticles are more efficient.

ASSOCIATED CONTENT

Supporting Information

The supporting information is available free of charge.

Graphical description of the electrospinning setup; photothermal heterodyne images of the substrates; polyacrylonitrile fiber characteristics.

ACKNOWLEDGMENT

The work was funded through award CHE-2103725 from the National Science Foundation. We acknowledge resources from the Campus Microscopy and Imaging Facility (CMIF) and the OSU Comprehensive Cancer Center (OSUCCC) Microscopy Shared Resource (MSR), The Ohio State University. This facility is supported in part by grant P30 CA016058, through the National Cancer Institute.

ABBREVIATIONS

LSPR, localized surface plasmon resonance; **PAN**, polyacrylonitrile; **PHI**, photothermal heterodyne imaging; **SERS**, surface enhanced Raman spectroscopy

REFERENCES

(1) Gao, Q.; Agarwal, S.; Greiner, A.; Zhang, T. Electrospun Fiber-Based Flexible Electronics: Fiber Fabrication, Device Platform, Functionality Integration and Applications. *Prog. Mater. Sci.* **2023**, 101139. https://doi.org/10.1016/j.pmatsci.2023.101139.

(2) Chee, W. K.; Lim, H. N.; Zainal, Z.; Harrison, I.; Huang, N. M.; Andou, Y.; Chong, K. F.; Pandikumar, A. Electrospun Nanofiber Membranes as Ultrathin Flexible Supercapacitors. *RSC Adv.* **2017**, *7* (20), 12033–12040. https://doi.org/10.1039/C7RA00406K.

(3) Miyamoto, A.; Lee, S.; Cooray, N. F.; Lee, S.; Mori, M.; Matsuhisa, N.; Jin, H.; Yoda, L.; Yokota, T.; Itoh, A.; Sekino, M.; Kawasaki, H.; Ebihara, T.; Amagai, M.; Someya, T. Inflammation-Free, Gas-Permeable, Lightweight, Stretchable on-Skin Electronics with Nanomeshes. *Nat. Nanotechnol.* **2017**, *12* (9), 907–913. https://doi.org/10.1038/nnano.2017.125.

(4) Zhai, Y.; Liu, H.; Li, L.; Yu, J.; Ding, B. Electrospun Nanofibers for Lithium-Ion Batteries. In *Electrospinning: Nanofabrication and Applications*; Elsevier, 2019; pp 671–694. https://doi.org/10.1016/B978-0-323-51270-1.00022-4.

(5) Kalluri, S.; Pang, W. K.; Seng, K. H.; Chen, Z.; Guo, Z.; Liu, H. K.; Dou, S. X. One-Dimensional Nanostructured Design of $Li_{1+x}(Mn_{1/3}Ni_{1/3}Fe_{1/3})O_2$ as a Dual Cathode for Lithium-Ion and Sodium-Ion Batteries. *J. Mater. Chem. A* **2015**, *3* (1), 250–257. https://doi.org/10.1039/C4TA04271A.

(6) Jayaraman, S.; Aravindan, V.; Suresh Kumar, P.; Ling, W. C.; Ramakrishna, S.; Madhavi, S. Synthesis of Porous LiMn2O4 Hollow Nanofibers by Electrospinning with Extraordinary Lithium Storage Properties. *Chem. Commun.* **2013**, *49* (59), 6677. https://doi.org/10.1039/c3cc43874k.

(7) Fu, Z.-W.; Ma, J.; Qin, Q.-Z. Nanostructured LiCoO2 and LiMn2O4 Fibers Fabricated by a High Frequency Electrospinning. *Solid State Ion.* **2005**, *176* (17–18), 1635–1640. https://doi.org/10.1016/j.ssi.2005.04.012.

(8) Lu, T.; Olesik, S. V. Electrospun Nanofibers as Substrates for Surface-Assisted Laser Desorption/Ionization and Matrix-Enhanced Surface-Assisted Laser Desorption/Ionization Mass Spectrometry. *Anal. Chem.* **2013**, *85* (9), 4384–4391. https://doi.org/10.1021/ac303292e.

(9) Bian, J.; Olesik, S. V. Ion Desorption Efficiency and Internal Energy Transfer in Polymeric Electrospun Nanofiber-Based Surface-Assisted Laser Desorption/Ionization Mass Spectrometry. *Anal. Bioanal. Chem.* **2020**, *412* (4), 923–931. https://doi.org/10.1007/s00216-019-02315-x.

(10) Bian, J.; Olesik, S. V. Polyvinylpyrrolidone Composite Nanofibers as Efficient Substrates for Surface-Assisted Laser Desorption/Ionization Mass Spectrometry. *Int. J. Mass. Spectrom.* **2020**, *448*, 116253. https://doi.org/10.1016/j.ijms.2019.116253.

(11) Bian, J.; Olesik, S. V. Surface-Assisted Laser Desorption/Ionization Time-of-Flight Mass Spectrometry of Small Drug Molecules and High Molecular Weight Synthetic/Biological Polymers Using Electrospun Composite Nanofibers. *Analyst* **2017**, *142* (7), 1125–1132. https://doi.org/10.1039/C6AN02444K.

(12) Chae, A.; Lee, G.; Koh, D.-Y.; Yang, C.-M.; Lee, S.; Kim, Y.-K. Polyacrylonitrile-Based Carbon Nanofibers as a Matrix for Laser Desorption/Ionization Time-of-Flight Mass Spectrometric Analysis of Small Molecules under Both Positive and Negative Ionization Modes. *Anal. Bioanal. Chem.* **2021**, *413* (4), 1193–1202. https://doi.org/10.1007/s00216-020-03083-9.

(13) Li, S.; Cui, Z.; Li, D.; Yue, G.; Liu, J.; Ding, H.; Gao, S.; Zhao, Y.; Wang, N.; Zhao, Y. Hierarchically Structured Electrospinning Nanofibers for Catalysis and Energy Storage. *Compos. Commun.* **2019**, *13*, 1–11. https://doi.org/10.1016/j.coco.2019.01.008.

(14) Kim, J.; Kang, J.; Jeong, U.; Kim, H.; Lee, H. Catalytic, Conductive, and Transparent Platinum Nanofiber Webs for FTO-Free Dye-Sensitized Solar Cells. *ACS Appl. Mater. Interfaces* **2013**, *5* (8), 3176–3181. https://doi.org/10.1021/am400179j.

(15) Shao, L.; Xing, G.; He, L.; Chen, J.; Xie, H.; Liang, X.; Qi, C. Sulfonic Groups Functionalized Preoxidated Polyacrylonitrile Nanofibers and Its Catalytic Applications. *Appl. Catal. A Gen.* **2012**, *443–444*, 133–137. https://doi.org/10.1016/j.apcata.2012.07.034.

(16) Chuangchote, S.; Jitputti, J.; Sagawa, T.; Yoshikawa, S. Photocatalytic Activity for Hydrogen Evolution of Electrospun TiO $_2$ Nanofibers. *ACS Appl. Mater. Interfaces* **2009**, *1* (5), 1140–1143. https://doi.org/10.1021/am9001474.

(17) Pierini, F.; Lanzi, M.; Nakielski, P.; Pawłowska, S.; Urbanek, O.; Zembrzycki, K.; Kowalewski, T. A. Single-Material Organic Solar Cells Based on Electrospun Fullerene-Grafted Polythiophene Nanofibers. *Macromol.* **2017**, *50* (13), 4972–4981. https://doi.org/10.1021/acs.macromol.7b00857.

(18) Haghighat Bayan, M. A.; Afshar Taromi, F.; Lanzi, M.; Pierini, F. Enhanced Efficiency in Hollow Core Electrospun Nanofiber-Based Organic Solar Cells. *Sci Rep* **2021**, *11* (1), 21144. https://doi.org/10.1038/s41598-021-00580-4.

(19) Shi, X.; Zhou, W.; Ma, D.; Ma, Q.; Bridges, D.; Ma, Y.; Hu, A. Electrospinning of Nanofibers and Their Applications for Energy Devices. *J. Nanomater.* **2015**, *2015*, 1–20. https://doi.org/10.1155/2015/140716.

(20) Willets, K. A.; Van Duyne, R. P. Localized Surface Plasmon Resonance Spectroscopy and Sensing. *Annu. Rev. Phys. Chem.* **2007**, *58* (1), 267–297. https://doi.org/10.1146/annurev.physchem.58.032806.104607.

(21) Blackie, E. J.; Le Ru, E. C.; Etchegoin, P. G. Single-Molecule Surface-Enhanced Raman Spectroscopy of Nonresonant Molecules. *J. Am. Chem. Soc.* **2009**, *131* (40), 14466–14472. https://doi.org/10.1021/ja905319w.

(22) Etchegoin, P. G.; Le Ru, E. C. A Perspective on Single Molecule SERS: Current Status and Future Challenges. *Phys. Chem. Chem. Phys.* **2008**, *10* (40), 6079. https://doi.org/10.1039/b809196j.

(23) Le Ru, E. C.; Galloway, C.; Etchegoin, P. G. On the Connection between Optical Absorption/Extinction and SERS Enhancements. *Phys. Chem. Chem. Phys.* **2006**, *8* (26), 3083. https://doi.org/10.1039/b605292d.

(24) Brongersma, M. L.; Halas, N. J.; Nordlander, P. Plasmon-Induced Hot Carrier Science and Technology. *Nat. Nanotechnol.* **2015**, *10* (1), 25–34. https://doi.org/10.1038/nnano.2014.311.

(25) Ratchford, D. C. Plasmon-Induced Charge Transfer: Challenges and Outlook. *ACS Nano* **2019**, *13* (12), 13610–13614. https://doi.org/10.1021/acsnano.9b08829.

(26) Guglielmelli, A.; Pierini, F.; Tabiryan, N.; Umeton, C.; Bunning, T. J.; De Sio, L. Thermoplasmonics with Gold Nanoparticles: A New Weapon in Modern Optics and Biomedicine. *Adv. Photonics.* **2021**, *2* (8), 2000198. https://doi.org/10.1002/adpr.202000198.

(27) Manjavacas, A.; Liu, J. G.; Kulkarni, V.; Nordlander, P. Plasmon-Induced Hot Carriers in Metallic Nanoparticles. *ACS Nano* **2014**, *8* (8), 7630–7638. https://doi.org/10.1021/nn502445f.

(28) Furube, A.; Hashimoto, S. Insight into Plasmonic Hot-Electron Transfer and Plasmon Molecular Drive: New Dimensions in Energy Conversion and Nanofabrication. *NPG Asia Mater* **2017**, *9* (12), e454–e454. https://doi.org/10.1038/am.2017.191.

(29) Kwasnieski, D. T.; Wang, H.; Schultz, Z. D. Alkyl-Nitrile Adlayers as Probes of Plasmonically Induced Electric Fields. *Chem. Sci.* **2015**, *6* (8), 4484–4494. https://doi.org/10.1039/C5SC01265A.

(30) Oklejas, V.; Sjostrom, C.; Harris, J. M. SERS Detection of the Vibrational Stark Effect from Nitrile-Terminated SAMs to Probe Electric Fields in the Diffuse Double-Layer. *J. Am. Chem. Soc.* **2002**, *124* (11), 2408–2409. https://doi.org/10.1021/ja017656s.

(31) Wright, D.; Sangtarash, S.; Mueller, N. S.; Lin, Q.; Sadeghi, H.; Baumberg, J. J. Vibrational Stark Effects: Ionic Influence on Local Fields. *J. Phys. Chem. Lett.* **2022**, *13* (22), 4905–4911. https://doi.org/10.1021/acs.jpclett.2c01048.

(32) Marr, J. M.; Schultz, Z. D. Imaging Electric Fields in SERS and TERS Using the Vibrational Stark Effect. *J. Phys. Chem. Lett.* **2013**, *4* (19), 3268–3272. https://doi.org/10.1021/jz401551u.

(33) El-Khoury, P. Z.; Schultz, Z. D. From SERS to TERS and Beyond: Molecules as Probes of Nanoscopic Optical Fields. *J. Phys. Chem. C* **2020**, *124* (50), 27267–27275. https://doi.org/10.1021/acs.jpcc.0c08337.

(34) Wang, H.; Yao, K.; Parkhill, J. A.; Schultz, Z. D. Detection of Electron Tunneling across Plasmonic Nanoparticle–Film Junctions Using Nitrile Vibrations. *Phys. Chem. Chem. Phys.* **2017**, *19* (8), 5786–5796. https://doi.org/10.1039/C6CP08168A.

(35) Nelson, D. A.; Schultz, Z. D. The Impact of Optically Rectified Fields on Plasmonic Electrocatalysis. *Faraday Discuss.* **2019**, *214*, 465–477. https://doi.org/10.1039/C8FD00135A.

(36) Li, Z.; Aleshire, K.; Kuno, M.; Hartland, G. V. Super-Resolution Far-Field Infrared Imaging by Photothermal Heterodyne Imaging. *J. Phys. Chem. B* **2017**, *121* (37), 8838–8846. https://doi.org/10.1021/acs.jpcb.7b06065.

(37) Mawatari, K.; Kitamori, T.; Sawada, T. Individual Detection of Single-Nanometer-Sized Particles in Liquid by Photothermal Microscope. *Anal. Chem.* **1998**, *70* (23), 5037–5041. https://doi.org/10.1021/ac980250m.

(38) Berciaud, S.; Cognet, L.; Blab, G. A.; Lounis, B. Photothermal Heterodyne Imaging of Individual Nonfluorescent Nanoclusters and Nanocrystals. *Phys. Rev. Lett.* **2004**, *93* (25), 257402. https://doi.org/10.1103/PhysRevLett.93.257402.

(39) Zeng, Z.-C.; Wang, H.; Johns, P.; Hartland, G. V.; Schultz, Z. D. Photothermal Microscopy of Coupled Nanostructures and the Impact of Nanoscale Heating in Surface-Enhanced Raman

Spectroscopy. *J. Phys. Chem. C* **2017**, *121* (21), 11623–11631. https://doi.org/10.1021/acs.jpcc.7b01220.

(40) Gaiduk, A.; Ruijgrok, P. V.; Yorulmaz, M.; Orrit, M. Detection Limits in Photothermal Microscopy. *Chem. Sci.* **2010**, *1* (3), 343. https://doi.org/10.1039/c0sc00210k.

(41) Zeng, Z.-C.; Schultz, Z. D. A Sensitive, Low Noise, DC to 12 MHz, Large Area Photodiode Preamplifier for Photothermal Heterodyne Imaging. *Rev. Sci. Instrum.* **2018**, *89* (8), 083105. https://doi.org/10.1063/1.5036626.

(42) Wang, Y.; Gao, Z.; Han, Z.; Liu, Y.; Yang, H.; Akkin, T.; Hogan, C. J.; Bischof, J. C. Aggregation Affects Optical Properties and Photothermal Heating of Gold Nanospheres. *Sci Rep* **2021**, *11* (1), 898. https://doi.org/10.1038/s41598-020-79393-w.

(43) Xu, M.-M.; Yuan, Y.-X.; Yao, J.-L.; Han, S.-Y.; Wang, M.; Gu, R.-A. Adsorption of 2-Amino-5-Cyanopyridine on a Gold Surface as Probed by Surface-Enhanced Raman Spectroscopy: Adsorption of 2-Amino-5-Cyanopyridine on a Gold Surface. *J. Raman Spectrosc.* **2011**, *42* (3), 324–331. https://doi.org/10.1002/jrs.2734.

(44) Berciaud, S.; Lasne, D.; Blab, G. A.; Cognet, L.; Lounis, B. Photothermal Heterodyne Imaging of Individual Metallic Nanoparticles: Theory versus Experiment. *Phys. Rev. B* **2006**, *73* (4), 045424. https://doi.org/10.1103/PhysRevB.73.045424.

(45) Mishra, S. R.; Ranjith, K.; Swathi, S. K.; Ramamurthy, P. C. Nanostructured Barbed Wire Architecturing of Organic Conducting Material Blends by Electrospinning. *Appl. Phys. Lett.* **2012**, *100* (1), 013302. https://doi.org/10.1063/1.3673620.

(46) Oliveira, J. E.; Mattoso, L. H. C.; Orts, W. J.; Medeiros, E. S. Structural and Morphological Characterization of Micro and Nanofibers Produced by Electrospinning and Solution Blow Spinning: A Comparative Study. *Adv. Mater. Sci. Eng.* **2013**, *2013*, 1–14. https://doi.org/10.1155/2013/409572.

(47) Wang, Z.; Sun, B.; Lu, X.; Wang, C.; Su, Z. Molecular Orientation in Individual Electrospun Nanofibers Studied by Polarized AFM–IR. *Macromol.* **2019**, *52* (24), 9639–9645. https://doi.org/10.1021/acs.macromol.9b01778.

(48) Zhou, Y.; Sha, Y.; Liu, W.; Gao, T.; Yao, Z.; Zhang, Y.; Cao, W. Hierarchical Radial Structure of Polyacrylonitrile Precursor Formed during the Wet-Spinning Process. *RSC Adv.* **2019**, *9* (30), 17051–17056. https://doi.org/10.1039/C9RA02125F.

(49) Li, D.; Kaner, R. B. Shape and Aggregation Control of Nanoparticles: Not Shaken, Not Stirred. *J. Am. Chem. Soc.* **2006**, *128* (3), 968–975. https://doi.org/10.1021/ja056609n.

(50) Li, Z.; Huang, H.; Wang, C. Electrostatic Forces Induce Poly(Vinyl Alcohol)-Protected Copper Nanoparticles to Form Copper/Poly(Vinyl Alcohol) Nanocables via Electrospinning. *Macromol. Rapid Commun.* **2006**, *27* (2), 152–155. https://doi.org/10.1002/marc.200500627.

(51) Liu, Y.; Chen, Q.; Cullen, D. A.; Xie, Z.; Lian, T. Efficient Hot Electron Transfer from Small Au Nanoparticles. *Nano Lett.* **2020**, *20* (6), 4322–4329. https://doi.org/10.1021/acs.nanolett.0c01050.

(52) Song, J.; Long, J.; Liu, Y.; Xu, Z.; Ge, A.; Piercy, B. D.; Cullen, D. A.; Ivanov, I. N.; McBride, J. R.; Losego, M. D.; Lian, T. Highly Efficient Plasmon Induced Hot-Electron Transfer at Ag/TiO $_2$ Interface. *ACS Photonics* **2021**, *8* (5), 1497–1504. https://doi.org/10.1021/acsphotonics.1c00321.

(53) Nelson, D. A.; Schultz, Z. D. Influence of Optically Rectified Electric Fields on the Plasmonic Photocatalysis of 4-Nitrothiophenol and 4-Aminothiophenol to 4,4-Dimercaptoazobenzene. *J. Phys. Chem. C* **2018**, *122* (15), 8581–8588. https://doi.org/10.1021/acs.jpcc.8b00662.

(54) Solati, E.; Dorranian, D. Comparison Between Silver and Gold Nanoparticles Prepared by Pulsed Laser Ablation in Distilled Water. *J Clust Sci* **2015**, *26* (3), 727–742. https://doi.org/10.1007/s10876-014-0732-2.

(55) Besteiro, L. V.; Kong, X.-T.; Wang, Z.; Hartland, G.; Govorov, A. O. Understanding Hot-Electron Generation and Plasmon Relaxation in Metal Nanocrystals: Quantum and Classical Mechanisms. *ACS Photonics* **2017**, *4* (11), 2759–2781. https://doi.org/10.1021/acsphotonics.7b00751.

(56) Lee, S. A.; Link, S. Chemical Interface Damping of Surface Plasmon Resonances. *Acc. Chem. Res.* **2021**, *54* (8), 1950–1960. https://doi.org/10.1021/acs.accounts.0c00872.

(57) Lee, S.-H.; Jo, J.-S.; Park, J. H.; Lee, S. W.; Jang, J.-W. A Hot-Electron-Triggered Catalytic Oxidation Reaction of Plasmonic Silver Nanoparticles Evidenced by Surface Potential Mapping. *J. Mater. Chem. A* **2018**, *6* (42), 20939–20946. https://doi.org/10.1039/C8TA07179A.

(58) Kazuma, E.; Lee, M.; Jung, J.; Trenary, M.; Kim, Y. Single-Molecule Study of a Plasmon-Induced Reaction for a Strongly Chemisorbed Molecule. *Angew Chem Int Ed* **2020**, *59* (20), 7960–7966. https://doi.org/10.1002/anie.202001863.

(59) Konstantopoulos, G.; Soulis, S.; Dragatogiannis, D.; Charitidis, C. Introduction of a Methodology to Enhance the Stabilization Process of PAN Fibers by Modeling and Advanced Characterization. *Mater.* **2020**, *13* (12), 2749. https://doi.org/10.3390/ma13122749.

(60) Xue, G.; Dong, J.; Zhang, J. SERS Studies of Polymers on Metal Surfaces. 4. Cyclization and Graphitization of Polyacrylonitrile on Rough Silver Surfaces. *Macromol.* **1992**, *25* (21), 5855–5857. https://doi.org/10.1021/ma00047a044.

TOC Graphic